Influence of microstructure and manganese sulfides on corrosion resistance of selective laser melted 17-4 PH stainless steel in acidic chloride medium

Michella Alnajjar, Frédéric Christien, Vincent Barnier, Cédric Bosch, Krzysztof Wolski, A. Dominic Fortes, Mark Telling

Influence of microstructure and manganese sulfides on corrosion resistance of selective laser melted 17-4 PH stainless steel in acidic chloride medium.

Michella Alnajjar[a], Frédéric Christien[a], Vincent Barnier[a], Cédric Bosch[a], Krzysztof Wolski[a], A. Dominic Fortes[b], Mark Telling[c]

[a] Mines Saint-Etienne, Univ Lyon, CNRS, UMR 5307 LGF, Centre SMS, F - 42023 Saint-Etienne France

[b] ISIS Facility, Rutherford Appleton Laboratory, Chilton, OX11 0QX, UK

[c] Department of Materials, University of Oxford, Parks Road, Oxford, UK

The corrosion resistance of 17-4PH stainless steel obtained by Selective Laser Melting was investigated. It was found that the as-built SLM-ed steel was entirely ferritic, not martensitic as expected. Re-austenitized SLM-ed steel recovered the martensitic microstructure. The two SLM-ed steels (as-built and re-austenitized) had the same general corrosion resistance which was correlated with their similar chemical composition. The martensitic re-austenitized SLM-ed steel had superior general corrosion behavior than the wrought martensitic steel. This was due to the nearly absence of MnS inclusions in the re-austenitized SLM-ed steel, while their presence in the wrought steel destabilized the passive film.

Keywords: 17-4 PH stainless steel; Selective Laser Melting; Microstructure; Corrosion properties; MnS inclusions

Introduction

Stainless steels are widely used in a variety of applications such as food processing, petrochemical plants and transportation industries, due to their high strength and good corrosion resistance. Their favorable corrosion properties are due to the presence of more than 11% chromium content by mass which allows for an adherent protective chromium oxide surface film to be formed [1]. 17-4 PH is a precipitation hardenable stainless steel that contains 15-17.5 wt.% of Cr and 3-5 wt.% of Ni. It usually has a martensitic microstructure and can be hardened by copper precipitates through aging treatments [2–4]. The corrosion resistance of this steel has been a subject of several studies that dealt with general corrosion, pitting, hydrogen embrittlement, and stress corrosion cracking. It was found that 17-4 PH steel was susceptible to both general and pitting corrosion in aqueous environment [5–7]. Pitting corrosion induced by a sulfuric and chloride acidic medium initiated at the MnS inclusions [6,7].

MnS inclusions have been known to be preferential sites for pit initiation in stainless steels in chloride containing solutions. They form weak points at the surface of a stainless steel because they are not protected by a passive oxide film [8]. Thus, chloride ions are adsorbed onto the sulfide inclusions, leading to the dissolution of the sulfide ions. The dissolution occurs according to the following reactions [9,10]:

$$MnS + 3H_2O \rightarrow Mn^{2+} + HSO_3^- + 5H^+ + 6e^- \quad \text{(Eq. 1)}$$

$$HSO_3^- + 5H^+ + 4e^- \rightarrow S + 3H_2O \quad \text{(Eq. 2)}$$

The resulting sulfur species released from the reaction are deposited in the vicinity of the inclusion. The dissolution of the MnS inclusion is accompanied by a decrease in pH, formation of a salt film and deposition of a sulfur layer. As a result, re-passivation will be impeded and acceleration of pit propagation will take place [8,10–15]. It has been reported that the stability of the pit is mainly related to the size, shape and orientation of the sulfide inclusions [14–16]. Furthermore, E. William *et al.* [17] demonstrated that a chromium depleted zone developed in the region adjacent to the MnS inclusion. In his analysis, this zone contributed to the increase of the dissolution rate. However, this Cr-depleted zone was not observed by other authors [18,19] and leaves the question of its presence ambiguous. On these bases, MnS inclusions must be controlled in stainless steels in order to minimize the pitting attacks. Indeed, an enhancement of pitting resistance after a laser surface melting treatment has been reported.

This was attributed to the redistribution, or elimination, of MnS inclusions caused by the surface treatment [15,20,21]. It is important to note that the majority of these studies focused on the effect of MnS inclusions on the corrosion resistance in austenitic stainless steel. Little attention was paid to their effect in ferritic and martensitic stainless steels.

Recently, stainless steels have been produced by additive manufacturing (AM) techniques, in particular the selective laser melting (SLM) process. AM consists of adding material layer by layer according to a computer-aided design (CAD) in order to create a three-dimensional object [22–24]. The microstructures of stainless steels obtained from AM have been the subject of many researches [25–29]. It has been shown that their microstructures can be very different from their wrought counterparts which present an anisotropic structure exhibiting dissimilar phase compositions. Such discrepancy was correlated to the high cooling rates that can be achieved during fabrication (10^5-10^6 K/s). Since the properties of the passive film vary with both composition and microstructure, the material is expected to have different corrosion behavior. In addition, AM stainless steels were free from MnS inclusions due to insufficient time for nucleation [30]. The absence of inclusions has been proven to be beneficial for the corrosion resistance of stainless steels. This was confirmed by authors who studied the corrosion behavior of austenitic stainless steel fabricated by AM. The AM material exhibited better electrochemical properties than the wrought steel [30–32]. In addition, M. R. Stoudt *et al.* reported an improved pitting corrosion of the AM 17-4 PH steel after a solution heat treatment. This improvement was associated with finer martensite lath, redistributed NbC precipitates and a more stable passive film [33]. However, it has also been reported that the enhanced corrosion of the AM 17-4 PH steel is due to the presence of porosity [34].

There have been limited number of studies concerning the corrosion behavior of AM 17-4 PH steel. As a result, and to further current understanding, this study focuses on the electrochemical characteristics of 17-4 PH steel fabricated by SLM in chloride containing acidic medium. A correlation between the corrosion behavior and the microstructure was made. Moreover, a comparison was also made with respect to the wrought material.

Experimental procedure

Materials

The materials used in this study were wrought and SLM-ed 17-4 PH stainless steels. The wrought material was a commercial bar from UGINE (cast # 818025). It was studied after a solution heat treatment at 1050 °C for 1 h followed by a water quench. Concerning the SLM-ed 17-4 PH steel, parts were cut from cylinders having 16 mm diameter and 105 mm length. They were fabricated in an SLM machine of type EOS M270. The fabrication was done in an argon purging environment. The longitudinal axis of the cylinder was horizontal perpendicular to the building direction Z. The SLM-ed material was studied both in the as-built condition and after a re-austenization heat treatment at 1050 °C for 1 h followed by a water quench. The plane used in the corrosion experiments was the (Y-Z) plane which is parallel to the build direction, Z. The chemical composition of both materials is given in Table 1. The full composition of the wrought material is indicated (data from the steel provider) in the first line of Table 1. Additional measurements were conducted on both wrought and SLM-ed materials (lines 2 and 3 of Table 1). These measurements were carried out using X-ray fluorescence (XRF) (FISCHERSCOPE X-Ray XAN-FD) for elements Ni, Cr and Cu, and using combustion elemental analysis (CEA) for C, S (LECO CS 444/LS), N and O (LECO TC-436).

Table 1: Chemical composition (wt. %) of wrought and SLM-ed 17-4 PH stainless steels

17-4 PH		C	Ni	Si	P	Mn	Cr	Cu	S	N	O	Nb	Fe
Wrought	Provider Data sheet	0.031	4.82	0.31	0.016	0.81	15.61	3.12	0.02	-	-	0.21	Bal.
	XRF/CEA	0.026	4.95	-	-	-	16.18	3.09	0.021	0.033	0.007	-	Bal.
SLM-ed	XRF/CEA	0.03	4.16	-	0.008	-	16.11	3.73	0.003	0.033	0.046	0.3	Bal.

Microstructural characterization

For microstructural characterization, scanning electron microscopy (SEM Zeiss SUPRA55VP) was used for both electron backscatter diffraction (EBSD) and energy dispersive spectroscopy (EDS). For both modes, the SEM was operated at 20 kV. For the EBSD preparation, samples were polished down to 1200 grit, followed by

electropolishing using 94% ethanol + 6% perchloric acid as electrolyte at 25 V for 60 s. For EDS, samples were only polished up to a 0.25 µm diamond finish.

The size, density and volume fraction of MnS inclusions were estimated from the EDS maps and the porosities from the optical micrographs, by using the image processing program ImageJ. Neutron diffraction was performed using the high-resolution powder diffractometer, HRPD, at the ISIS neutron and muon spallation facility, Rutherford Appleton Laboratory (RAL), UK [35]. Using the instrument's standard 30-130 ms time-of-flight measurement window, the range of interplanar distances, or d-spacings, examined with highest-resolution backscattering detectors was between 0.065 and 0.265 nm. Data were normalized to the incident spectrum and corrected for instrumental efficiency using V:Nb null-scattering standard. Patterns were acquired at room temperature for the three studied materials. The dislocation density ρ can be correlated to the average peak broadening $\Delta d/d$ (where d is the interplanar spacing) using the following Stibitz equation (Eq. 3) [36,37]:

$$\boldsymbol{\rho = \frac{3E}{\mu b^2(1+2\upsilon^2)}(\Delta d/d)^2} \quad \text{(Eq. 3)}$$

here E is the Young's modulus, µ is the shear modulus with $E/\mu \approx 2.5$ for the materials studied here. The burger vector b is approximately equal to 0.249 nm and the Poisson's coefficient υ is equal to 0.25. The peak broadening Δd was determined using a deconvolution method. The determination of $\Delta d/d$ was done on four peaks corresponding to the crystallographic planes (220), (211), (200) and (110) and then their average was computed. This is the same methodology that was already used on 17-4 PH steel in a previous study by Christien *et al* [38]. Furthermore, the mass fraction of the austenite present in the three studied materials was determined by the Rietveld structure refinement method applied to the neutron powder diffraction data using GSAS/Expgui [39,40].

Surface analyses were performed using X-Ray Photoelectron Spectroscopy (XPS) with a Thermo VG Thetaprobe spectrometer instrument. Analyses were carried out with a focused monochromatic AlKα source ($h\upsilon$ = 1486.68 eV, 400 µm spot size) and a concentric hemispherical analyzer operating in constant ΔE mode. The energy scale was calibrated with sputter-cleaned pure reference samples of Au, Ag and Cu with Au4f7/2, Ag3d5/2 and Cu3p3/2 positioned at binding energies of 83.98, 386.26 and 932.67 eV respectively. In order to detect the presence of

chemical species containing sulfur at the surface of samples, narrow scans were recorded for S2p peak with a step size of 0.1 eV and a pass energy of 50 eV. This pass energy gives a width of the Ag3d5/2 peak measured on a sputter cleaned pure Ag sample of 0.55 eV. These scans were performed with the analyzer operating in standard mode but also in angle resolved mode using the ability of the spectrometer to collect simultaneously several photo-electron emission angles over a 60° range without tilting the sample. The S2p experimental curves were adjusted with components using lineshapes consisting of a convolution product of a Gaussian function (75%) and Lorentzian function (25%) for components associated with the sulfate and sulfite species and asymmetric lineshapes for components associated with sulfide species.

Electrochemical measurements

Electrochemical measurements were performed on the three materials using a VoltaLab PST 006 potentiostat. They were carried out using a typical three-electrode cell. The working electrodes were wrought and SLM-ed ((Y-Z) plane in the as-built and re-austenitized condition) materials. The counter electrode used to provide the applied current was made of platinum. Potentials were measured with reference to the saturated calomel reference electrode (SCE). Specimens were polished with a 0.25 µm diamond paste to produce a mirror like surface finish. They were rinsed and cleaned with water and ethanol. In order to have the same surface condition at the beginning of each test, the specimens were left after polishing for one day in air to form a similar passive film. The surface exposed to the solution had an area of 0.5 - 0.8 cm^2. The test solution was deionized water with 30 g/L NaCl and was deaerated using a continuous flux of N_2 gas for 24 h before introducing the specimen and throughout the experiment. The studied pH were varied between 1.5, 2.5 and 3.5 with an error of ± 0.05. They were adjusted by adding some droplets of hydrochloric acid and sodium hydroxide in the solution. The temperature was maintained at room temperature (20°C ± 2°C). The open circuit potential was measured for an immersion time of 5 h. The anodic scans were repeated 3 times on each specimen, and at each condition, to ensure the good reproducibility of the experiments. Between two anodic scans, samples were grounded to remove the pitting and then re-polished. The polarization curves shown in this paper are the mean of the three curves measured (the raw data of each curve are provided as supplementary material). The scans started from -600 mV vs. SCE, slightly in the cathodic region, and continued until an anodic current of 1 mA was reached. The scan rate applied during testing was 0.1 mV/min.

Results and discussion

Microstructure

The wrought 17-4 PH steel was studied after a solution heat treatment at 1050 °C for 1 h followed by a water quench. The microstructure obtained was a fully martensitic structure, as shown by the EBSD map in Fig. 1a. The laths of martensite are gathered into different packets inside the same prior austenitic grain. The average martensitic grain size was measured using the intercept method and is given in Table 2. In addition, a reconstruction of the former austenitic grains was applied to the EBSD map using an automatic iterative method based on the austenite/martensite orientation relationships developed by T. Nyyssönen [41]. Fig. 1d reveals the map of the reconstructed former austenite grains. Their average size was measured using the same intercept method and was found to be approximately 19.8 µm. The EDS measurements in Fig. 2a reveal a homogeneous distribution of elements and the presence of circular MnS and NbS inclusions of approximately 1 µm in diameter, as well as some oxides. Table 2 indicates the inclusions density, size and volume fraction estimated from the EDS maps. In addition, NbC precipitates are also possibly present in this material. These observations are typically found in the wrought 17-4 PH steel after this heat treatment.

In contrast to the wrought steel, the microstructure of as-built SLM-ed 17-4 PH steel (Fig. 1b) does not show a typical martensitic microstructure with packets and blocks. The microstructure consists mainly of coarse grains having an average grain size of 9.2 µm. Since the majority phase has a BCC structure, it is deduced that the as-built SLM-ed 17-4 PH steel has a ferritic microstructure, more specifically δ ferrite. This ferritic microstructure has been observed and discussed in details in a previous study [29]. Furthermore, some authors also reported similar ferritic microstructures in SLM-ed 17-4 PH steel [42,43]. This ferritic microstructure is due the high cooling and heating rates experienced during SLM which do not allow the austenite phase time to be formed. Thus, the δ ferrite formed during solidification does not undergo any further metallurgical transformation. This can be described as if delta ferrite has by-passed the austenite phase. In addition, during SLM construction the steel will exhibit multiple thermal cycles and the temperatures can reach the austenite phase stability range. Thus, there might be a

possibility for the austenite to form. However, due to the extremely high thermal rates the austenite formation will also be suppressed and the same by-passing phenomenon will occur. Thus, the delta ferrite will be maintained during the SLM process until the building of the part is completed. Fig. 2b depicts the EDS measurements of the as-built material. It reveals a homogeneous distribution of elements. This homogeneity of elements is correlated to a planar solidification front characteristic of very high cooling rates, as the case with SLM fabrication. The planar interface between solid and liquid state is an indication of a diffusionless solidification. Unlike the wrought material, no MnS inclusions or NbC precipitates were visible. This can be due to the high cooling and heating kinetics that suppressed their nucleation and growth. Only widely-spaced oxides can be observed.

After re-austenization (at 1050 °C for 1 h followed by a water quench), the SLM-ed material presents a martensitic microstructure, as shown in the EBSD map in Fig. 1c. This implies that the delta ferrite-to-austenite transformation took place during heating and subsequent holding for 1 h at 1050 °C, and that the austenite-to-martensite transformation occurred during cooling, resulting in the observed microstructure. From the EBSD map, it can be seen that the laths of martensite are gathered into packets inside prior austenitic grains. The martensitic grain size was measured using the intercept method and is given in Table 2. Fig. 1e shows the map of the reconstructed former austenitic grains. The reconstruction was applied to the EBSD map by using the same automatic iterative method that was applied to the EBSD map of the wrought steel. The average former austenitic grain size was approximated 12.5 µm by using the intercept method. From Table 2, it can be seen that the martensitic re-austenitized SLM-ed steel has the smallest grain size. Fig. 2c shows a homogeneous distribution of elements. In addition to rare oxides particles found initially in this steel, MnS and NbS inclusions, as well as possible NbC precipitates, are formed during this treatment. Since these inclusions and precipitates were able to form during re-austenization, this confirms that the high cooling and heating rates have indeed inhibited their formation during the SLM process. Table 2 shows the MnS inclusions density, size and volume fraction. It can be seen that their density and size are less in the re-austenitized SLM-ed steel when compared to the wrought steel.

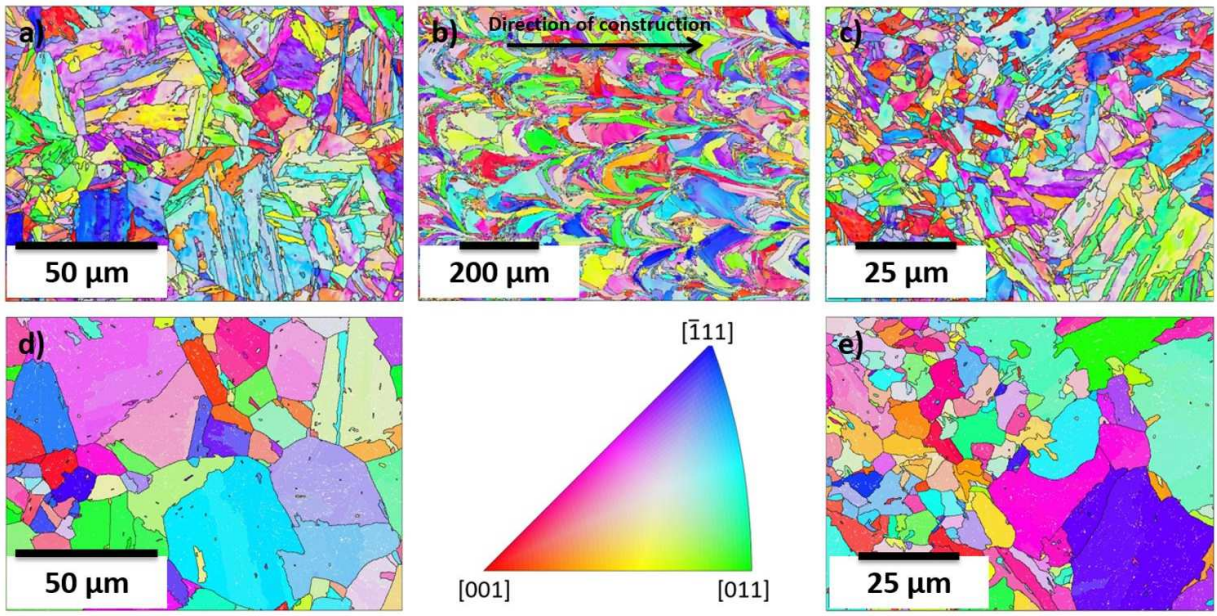

Fig. 1: EBSD orientation map of (a) wrought 17-4 PH steel showing a typical martensitic microstructure, (b) as-built SLM-ed 17-4 PH steel in the (Y-Z) plane showing coarse grain ferritic microstructure and (c) re-austenitized SLM-ed 17-4 PH steel showing martensitic microstructure. Prior austenitic grains reconstruction using the EBSD maps is presented in (d) for the wrought steel and in (e) for the re-austenitized SLM-ed steel (IPF coloring).

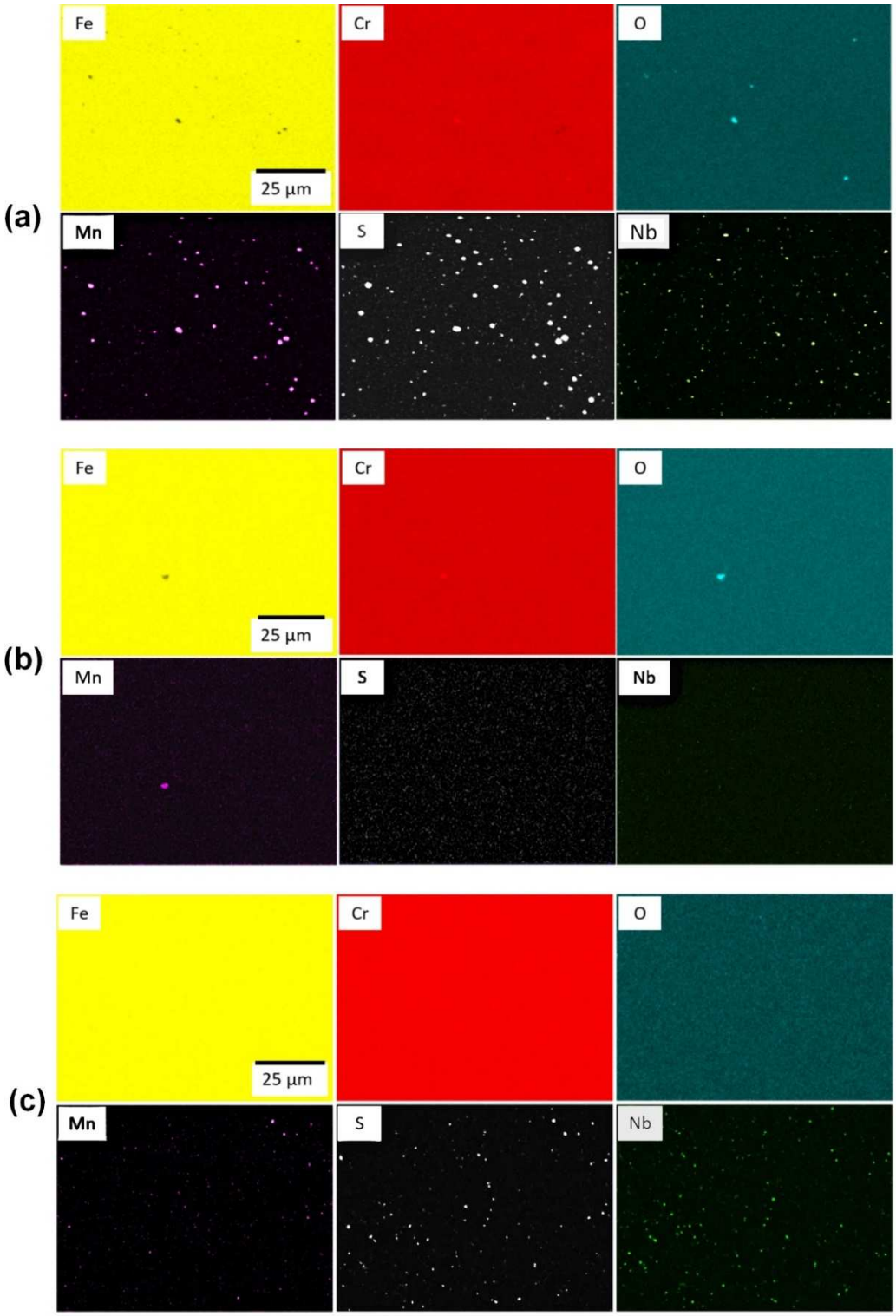

Fig. 2: EDS maps of Fe, Cr, Mn, S, O and Nb showing (a) homogeneous distribution with MnS and NbS inclusions, oxides and possibly NbC precipitates for wrought 17-4 PH steel, (b) homogeneous distribution with oxides for as-built SLM-ed 17-4 PH steel and (c) homogeneous distribution with MnS and NbS inclusions, oxides and possibly NbC precipitates for re-austenitized SLM-ed 17-4 PH steel.

Fig. 3 depicts the neutron diffraction pattern of the BCC plane (110) peak (ferrite and martensite) at room temperature for the three steels. It is seen that the BCC peak is larger in area for both martensitic steels (wrought and re-austenitized SLM-ed steels) in comparison with the ferritic as-built SLM-ed steel. From Eq. 3, the dislocation density was approximated and is given in Table 2. The dislocation density is almost the same for the martensitic steels (wrought and re-austenitized SLM-ed steels). These martensitic steels have higher dislocation density than the as-built SLM-ed steel. This observation is in agreement with several studies showing that the martensitic transformation results in a high dislocation density in the quenched state [44–46]. Furthermore, the austenite mass fraction of the three studied materials was approximated by applying Rietveld refinement method on the neutron diffraction data (Table 2). The as-built SLM-ed steel had the highest austenite content. While the wrought steel and re-austenitized SLM-ed steel had less than a 1% austenite mass fraction. The porosity in the materials was also measured and is given in Table 2. The wrought steel was free of porosity while both SLM-ed steels had a similar porosity characteristics.

Table 2: Microstructural features (grain size, MnS inclusions, dislocation density, porosity, austenite) of the three studied steels.

	Wrought	SLM as-built	SLM re-austenitized

Grain size (μm)		Martensitic: 3.3 Former austenitic: 19.8	Ferritic: 9.2	Martensitic: 2 Former austenitic: 12.5
MnS inclusions	Density: number/area (m^{-2})	$7.6\ 10^{9}$	0	$3.7\ 10^{9}$
	Size (μm)	1.0	0	0.5
	Volume fraction (%)	0.7	0	0.1
Dislocation density (m^{-2})		$\sim 6.0\ 10^{15}$	$\sim 1.0\ 10^{15}$	$\sim 7.0\ 10^{15}$
Porosity	Density: number/area (m^{-2})	0	$1.1\ 10^{8}$	$1.1\ 10^{8}$
	Size (μm)	0	4.4	4.4
	Volume fraction (%)	0	0.1	0.1
Austenite (%)		<1.0	9.2	<1.0

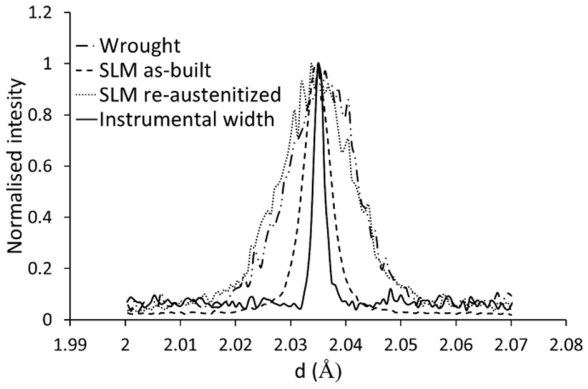

Fig. 3: Neutron diffraction pattern of the three studied materials showing a larger BCC (110) peak for both martensitic wrought steel and re-austenitized SLM-ed steels in comparison with the ferritic as-built SLM-ed steel. (d is the interplanar spacing)

Potentiodynamic measurements

Fig. 4 depicts the potentiodynamic plots of the SLM-ed steels in the as-built and re-austenitized conditions for different pH in deaerated 30 g/l NaCl solution. The polarization scan starts immediately at the immersion of the working electrode from -600 mV/ SCE (slightly cathodic potential) at 0.1 mV/min scan rate. For each pH, the corrosion potential for both SLM-ed steels is similar and varies between -405 and -455 mV/SCE. At this potential, the anodic dissolution and the cathodic reduction rates at the surface of the electrode are balanced and the sum of their respective density current is equal to zero. As the potential increases, the dissolution of the metal takes place characterized by an increase in current. This region is called the active region. For pH higher than 2.5, the anodic peak current density for both SLM-ed steels is smaller than 10 $\mu A/cm^2$ and the metal is considered passivated. The value of 10 $\mu A/cm^2$ is the critical active peak value above which the metal is considered as no longer passivated. This arbitrary value corresponds to a corrosion rate of 0.1 mm/year and is taken as the onset of a significant corrosion rate [47,48]. For pH equal to 1.5, the active peaks for the SLM-ed in the as-built and re-austenitized conditions were 45 $\mu A/cm^2$ and 60 $\mu A/cm^2$ respectively. These peaks are higher than 10 $\mu A/cm^2$ and the materials are no longer considered passivated in this potential range.

It can be concluded that the general corrosion behavior of the two steels is very similar (same corrosion potential and same pH of passivation). It should be noted that the two steels have different microstructures: the as built SLM-ed steel is ferritic, while the re-austenitized SLM-ed steel is martensitic. This leads to the conclusion that the microstructure did not have any effect on the general corrosion behavior. This similar corrosion behavior can be correlated to the identical chemical composition of the two steels that controlled the composition of the passive film and consequently its stability in the acidic chloride medium.

Concerning the pitting corrosion behavior at higher potential, the two steels had different pitting potentials. For all the pH, the pitting potential was higher for the as built SLM-ed steel than the re-austenitized one. Thus, the as built SLM-ed steel is more resistant to the pitting corrosion. The pitting corrosion normally initiates at some microstructural defects or discontinuities in the passive film caused by inclusions, grain boundaries and dislocations [49,50]. Since the re-austenitized SLM-ed steel has a martensitic structure, it has higher dislocation and grain boundary densities than the as-built SLM-ed steel (shown in Table 2) which will increase the probability of pit initiation. It is worth mentioning that there have been many studies concerning the effect of grain size on corrosion

resistance. However, their results are not conclusive. For ferrous alloys, in some cases, the refinement of grains was considered beneficial for pitting corrosion [51,52]. In other cases, it was detrimental [53–55]. Furthermore, to the author's knowledge, no work has been done concerning the effect of grain size on pitting corrosion in a martensitic stainless steel. In addition, the MnS inclusions present in the re-austenitized SLM-ed steel, which have been proven to be preferential sites for pitting, could be also the cause of the lower pitting potential. However, this assumption is questionable because, as it will be shown later, the MnS inclusions did not have any effect on the pitting potential of the wrought steel. On the other hand, since the porosity content is the same for both steels, it cannot account for the difference in pitting potential. As shown in Table 2, the austenite content was higher in the as-built SLM-ed steel. Thus, it seems that the austenite did not have any detrimental effect on the observed pitting potential.

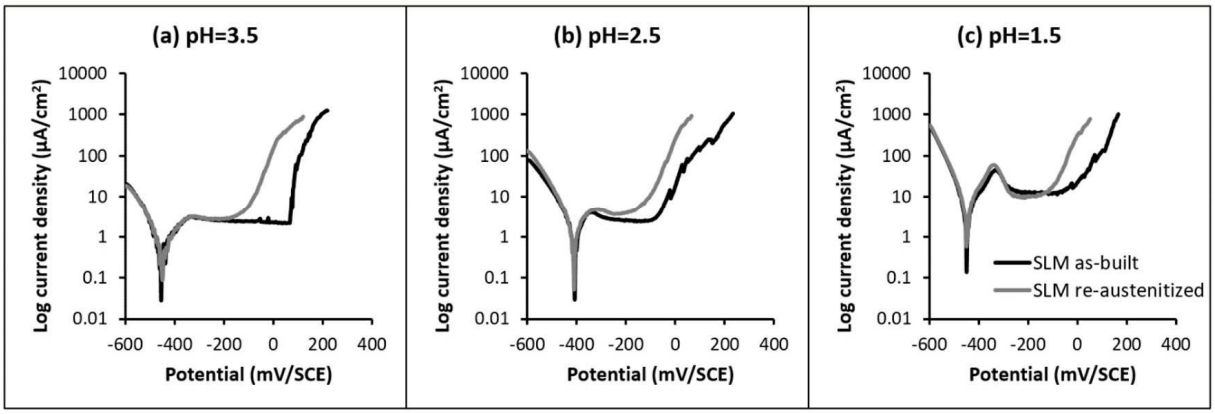

Fig. 4: Comparison of the electrochemical behavior of the as-built SLM-ed steel and the re-austenitized SLM-ed steel in 30g/l NaCl solution at (a) pH=3.5, (b) pH=2.5 and (c) pH=1.5.

Fig. 5 shows the polarization curves of the re-austenitized SLM-ed and the wrought steels at different pH in deaerated 30g/l NaCl solution. Similarly to Fig. 4 the polarization scan starts immediately at the immersion of the working electrode from -600 mV/ SCE (slightly cathodic potential) at 0.1 mV/min scan rate. The corrosion potential is different for the two steels. It tends to more noble values for the re-austenitized SLM-ed steel. In addition, it is noticed that at the corrosion potential the current density is almost ten times higher for the wrought steel. Furthermore, the general corrosion characterized by the anodic peak current density was more pronounced in the

wrought steel. At pH=3.5, both steels had an activation peak lower than 10 µA/cm^2 which means that they can be considered as passivated even close to the corrosion potential. At pH=2.5, the re-austenitized SLM-ed steel was still passivated while this wasn't the case for the wrought steel. The latter exhibited a very large active peak. As the pH decreased to 1.5, both steels were depassivated. However, the peak current density was significantly higher in intensity and much larger for the wrought steel.

It should be noted that both steels have almost similar martensitic structure. However, the sulfur content is much higher in the wrought steel (Table 1), which results in higher density and size of MnS inclusions (Table 2). Actually, MnS inclusions are not only possible preferential sites for pit initiation but also destabilize the passive film. This was proven by several studies, where authors found anodic activity in the vicinity of the MnS inclusions corresponding to the breakdown of passivity. It was explained by the deposition of sulfur species in the adjacent region that were liberated from the MnS dissolution. The deposited sulfur promoted the destabilization of the passive film [56–61]. Oudar *et al.* [61] studied the active/passive behavior of pure nickel related to the amount of adsorbed sulfur. They have found that the adsorbed sulfur had a catalytic effect on the rate of dissolution of metal in the active region of the anodic curve. Furthermore, they showed that there was a critical concentration of adsorbed sulfur, slightly lower than a monolayer, which totally inhibits the passivation of nickel alloy.

On the other hand, the pitting potential was not significantly different; it was even slightly higher in the wrought steel. Although the MnS content was far higher in the wrought steel, this did not have any strong influence on the pitting behavior. According to Eklund [62], MnS inclusions can only exist between pH 4.8 and 13.8. Since the anodic scan rate used during these tests was slow, it is possible that there was enough time for the MnS inclusions to dissolve completely and for its exposed surface to passivate before reaching the pitting potential. As a result, these inclusions did not affect the pitting resistance. Indeed, some authors reported that a preliminary electrochemical treatments were successful in removing the MnS inclusions leading to an improved pitting resistance [63,64]. One possible explanation for the slightly lower pitting potential for the re-austenitized SLM-ed steel would be its higher grain boundary density, since it has smaller grains, and the presence of porosities as shown in Table 2. This suggests that the grain boundaries and porosities could be sites for pit initiation in these steels.

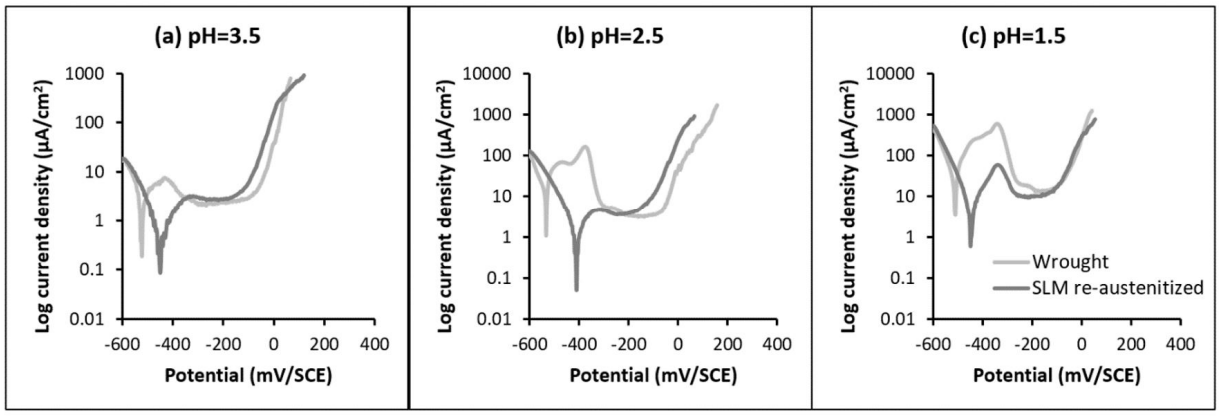

Fig. 5: Comparison of the electrochemical behavior of the wrought steel and the re-austenitized SLM-ed steel in 30g/l NaCl solution at (a) pH=3.5, (b) pH=2.5 and (c) pH=1.5.

Open circuit potential

The open circuit potential (OCP) of the three steels at pH equal to 2.5 is given in Fig. 6. The OCP was measured for 5 h. It is shown that at the beginning of immersion there is a sharp decrease of the OCP for all the steels. This is correlated to the dissolution of the passive film formed in contact with air [65]. After the sharp decrease of the OCP, the potential for both SLM-ed steels (as-built and re-austenitized) exhibit a slight increase with time of immersion. This increase of the OCP is an indication of a growing stable passive film and its enrichment in chromium oxide [66]. However, the wrought steel does not exhibit this increase of the OCP and the potential stabilizes after half an h to a less noble potential than the SLM-ed steels. This indicates that an unstable oxide film developed that does not have an effective protection.

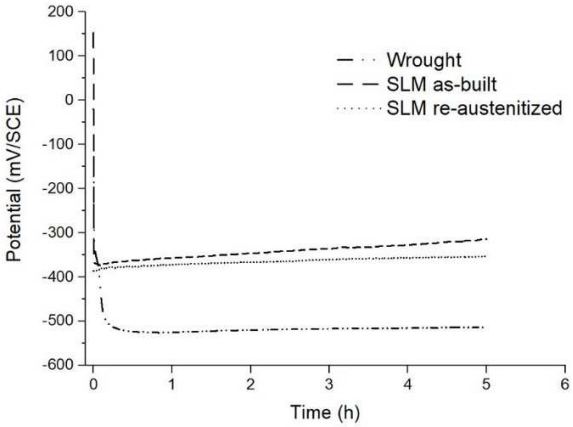

Fig. 6: OCP measurement over 5 h period at pH=2.5 for the three steels. The data shows a slight increase in OCP for the SLM-ed steels and a stabilisation at less noble potential for the wrought steel.

After the test at OCP for 5 h at pH equal to 2.5, the exposed surfaces were studied by optical microscopy (Fig. 7). Fig. 7b and Fig. 7c show the exposed surfaces of as-built and re-austenitized SLM-ed steels. They both present an intact surface with no evidence of generalized corrosion. Some porosities can be seen that were initially present in the SLM-ed steels before corrosion. In contrast, the exposed surface of the wrought steel in Fig. 7a was subjected to general corrosion. Small dark points that cover all the surface correspond to the dissolved MnS inclusions. The dissolution of MnS in stainless steels under free corrosion was reported by multiple authors [11,57,66]. As mentioned earlier, MnS inclusions are not stable below pH 4.8 [62]. Therefore, it is expected that MnS inclusions would dissolve at pH 2.5. These observations along with the OCP measurements confirm the results of the potentiodynamic scans at pH 2.5 that showed that the SLM-ed steels were passivated in contrast to the wrought steel.

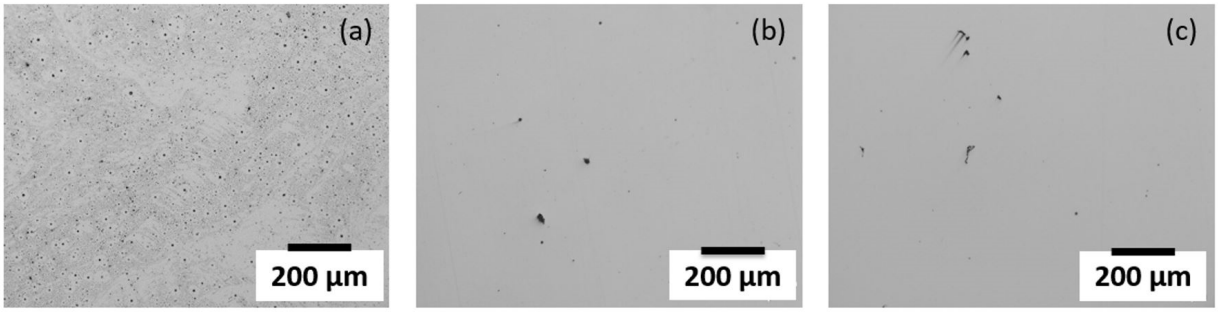

Fig. 7: Optical micrographs showing the exposed surface after OCP for 5 h of (a) the wrought steel, (b) as-built SLM-ed steel and (c) re-austenitized SLM-ed steel.

XPS measurements

XPS measurements were performed in order to confirm the presence of a sulfur enrichment on the surface resulting from MnS dissolution. Only the wrought steel was studied here. The surface states were studied in two conditions: after polishing to a mirror finish (polished) and after 24 h of immersion at OCP in a deaerated solution containing 30 g/l NaCl at pH=2.5 (exposed). Fig. 8a depicts the S 2p spectrum for both conditions. The polished surface had a small S2p peak at 161.55 eV. According to the literature, this component corresponds to MnS inclusions [67,68]. After immersion for 24 h, the total sulfur signal became higher by a factor of six compared to the initial polished surface. This indicates that a large part of the surface was covered by sulfur containing species. Thus, the corrosion of this steel (OCP for 24 h) resulted in an enrichment of sulfur species on the surface. In addition, three peaks, related to the S2p level, can be identified on the exposed surface. The peak at 161.7 eV corresponds to the sulfur deposited on the surface that formed sulfides like FeS, CrS and Cu_2S [69–72]. The peak at 166.6 eV is a typical value for sulfite ions, more specifically ferrous sulfite $FeSO_3$ [70,73]. The peak at 168.26 eV was found to correspond to ferrous sulfate $FeSO_4$ [57,71,74]. Fig. 8b shows the three components of S2p spectra of the exposed surface recorded in XPS angle resolved mode. For each component the ratio of the intensity at photoelectrons take-off angle of 25° to the one at 65° indicates how close chemical species are to the extreme surface. A "relative depth" d* of each component can be estimated using Eq. 4:

$$\boldsymbol{d^*} = \boldsymbol{d}\left[\left(\frac{\mathbf{1}}{\boldsymbol{\lambda cos(25)}} - \frac{\mathbf{1}}{\boldsymbol{\lambda cos(65)}}\right)\right] = -\mathbf{ln}\left(\frac{\boldsymbol{I_{65°}}}{\boldsymbol{I_{25°}}}\right) \quad \text{(Eq. 4)}$$

Where d is the depth of a given layer, λ is the electron inelastic mean free path (considered the same in all the layers), and $I_{25°}$ and $I_{65°}$ are the intensities of a given component at 25° and 65° take-off angle respectively. The relative depth, d*, is a dimensionless parameter that allows the localization of the different layers with respect to

each other. This relative depth is presented in Fig. 8c and indicates that the sulfate component seems to be located at the extreme surface. The sulfide is the deepest component and the sulfite is at an intermediate depth. This is in agreement with previous studies that demonstrated that the sulfate is located in the outer part of the passive film [57], while the sulfide is more profound [69]. Based on these observations, a schematic distribution of the sulfur species is proposed in Fig. 8d. Fig. 9 shows the secondary electron micrograph of the exposed surface of the wrought 17-4 PH steel along with its EDS maps of manganese and sulfur. The EDS maps don't show any MnS inclusions indicating their complete dissolution after 24 h of immersion at OCP in a deaerated solution containing 30 g/l NaCl at pH=2.5. These observations confirm that during immersion, the MnS inclusions dissolve and the sulfur liberated from the dissolution is deposited on the surface and changes the chemical composition of the passive film. Thus, it leads to a destabilization of the passive film, which is in agreement with previous studies on austenitic stainless steels [56–59]. This destabilization will result in the occurrence of general corrosion.

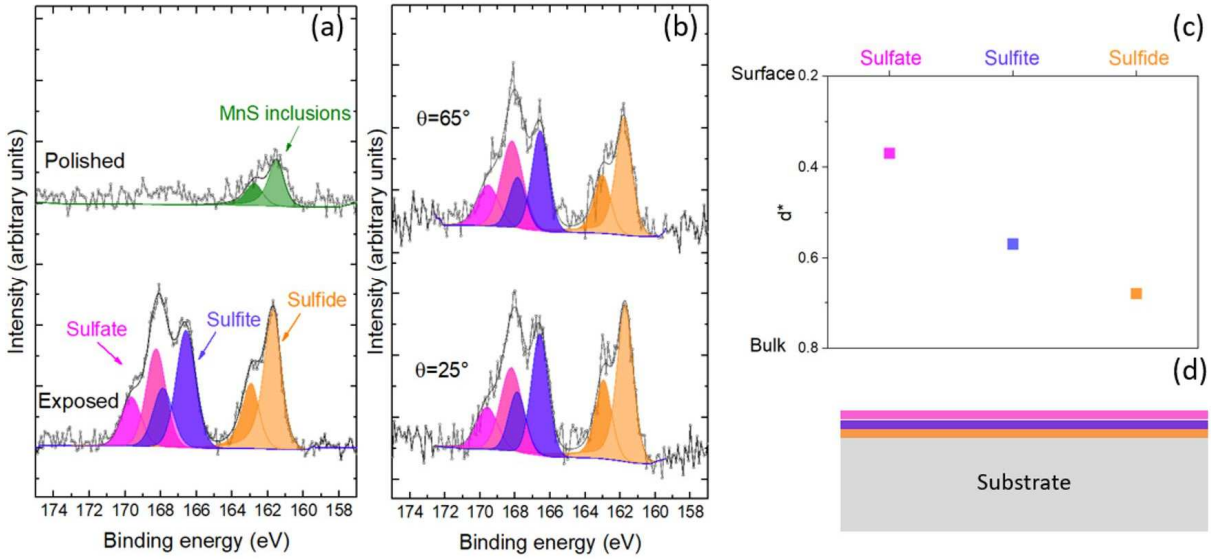

Fig. 8: (a) S2p spectra determined from XPS of the polished and exposed (24 h at OCP in 30 g/l NaCl at pH=2.5) surfaces of the wrought 17-4 PH steel (b) S2p angle-resolved XPS analyses of the exposed surface at two photoelectron escape angles (Θ=25° and Θ=65°), (c) depth plot based on the ratio of intensities at Θ=25° and Θ=65° using Eq. 4, (d) schematic distribution of the sulphur species related to each component.

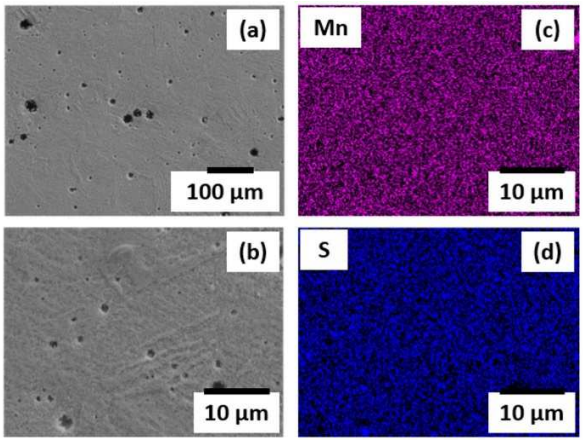

Fig. 9: (a) and (b) Secondary electron micrographs of the exposed surface of the wrought 17-4 PH steel. EDS maps of (c) manganese and (d) sulfur elements corresponding to image (b) showing a complete dissolution of MnS inclusions after 24 h at OCP in 30 g/l NaCl at pH=2.5.

Conclusion

The aim of this study was to determine the corrosion behavior of SLM-ed 17-4 PH steel by electrochemical characterization. A series of potentiodynamic scans were performed at three different pH in deaerated 30 g/l NaCl solution. Measurements were conducted on the SLM-ed steel in the as-built condition and after re-austenization treatment (both in the (Y-Z) plane) and on the wrought steel. The microstructure of the SLM-ed steel in the as-built condition was mostly ferritic and was due to the high cooling and heating rates that did not allow enough time for the austenite to be formed. As a result, the delta ferrite formed during solidification did not undergo any metallurgical transformation and was retained at room temperature. After re-austenization heat treatment, the SLM-ed steel was completely transformed into martensite. In addition, the wrought steel had a typical martensitic structure. The sulfur content that had a significant influence on the obtained results was higher in the wrought steel compared with the SLM-ed steels. Potentiodynamic measurements showed that:

1. The pH of depassivation was the same for the SLM-ed steel in the two conditions (as-built and re-austenitized) regardless of their microstructures. This suggests that the difference in microstructures had little effect on general corrosion resistance for both steels.

2. The pitting potential was higher in the as-built condition than the re-austenitized one. This was associated with the higher grain boundaries and dislocation densities.
3. The re-austenitized SLM-ed steel had a remarkably superior general corrosion resistance than the wrought steel. This was associated with the lower sulfur content, more specifically the lower MnS inclusion content in the re-austenitized SLM-ed steel. In the wrought steel, the dissolution of MnS inclusions led to a deposition of a sulfur rich layer in the adjacent regions that promoted the destabilization of the passive film and thus deteriorated the general corrosion resistance. The XPS measurements confirmed the formation of sulfur species on the surface of the wrought steel.
4. The wrought steel was slightly more resistant than the re-austenitized SLM-ed steel. The higher grain boundary density and the presence of porosities in the martensitic re-austenitized SLM-ed steel could contribute to this behavior.

Acknowledgments

The staff of the Pressure and Furnace Section at the ISIS facility, namely Chris Goodway, Paul Mclntyre and Adam Sears, are kindly acknowledged for their work in preparing and setting-up the equipment for the neutron diffraction tests. Tuomo Nyyssönen at Tampere University of Technology is acknowledged for supplying the code for the austenite grain reconstruction. The authors would like to acknowledge financial support from Institut CARNOT M.I.N.E.S (project #60678) and from LABEX MANUTECH-SISE (ANR-10-LABX-0075) of Université de Lyon, within the program “Investissements d’Avenir” (ANR-11-IDEX-0007) operated by the French National Research Agency (ANR).

References

[1] J.R. Davis, ASM International, eds., in: Stainless Steels, ASM International, Materials Park, Ohio, 1994: pp. 3–5.
[2] C.N. Hsiao, C.S. Chiou, J.R. Yang, Aging reactions in a 17-4 PH stainless steel, Materials Chemistry and Physics. 74 (2002) 134–142. https://doi.org/10.1016/S0254-0584(01)00460-6.
[3] W.D. Yoo, J.H. Lee, K.T. Youn, Y.M. Rhyim, Study on the Microstructure and Mechanical Properties of 17-4 PH Stainless Steel Depending on Heat Treatment and Aging Time, Solid State Phenomena. 118 (2006) 15–20. https://doi.org/10.4028/www.scientific.net/SSP.118.15.

[4] U.K. Viswanathan, S. Banerjee, R. Krishnan, Effects of aging on the microstructure of 17-4 PH stainless steel, Materials Science and Engineering: A. 104 (1988) 181–189. https://doi.org/10.1016/0025-5416(88)90420-X.
[5] B.C. Syrett, R. Viswanathan, S.S. Wing, J.E. Wittig, Effect of Microstructure on Pitting and Corrosion Fatigue of 17-4 PH Turbine Blade Steel in Chloride Environments, CORROSION. 38 (1982) 273–282. https://doi.org/10.5006/1.3577350.
[6] D. Nakhaie, M.H. Moayed, Pitting corrosion of cold rolled solution treated 17-4 PH stainless steel, Corrosion Science. 80 (2014) 290–298. https://doi.org/10.1016/j.corsci.2013.11.039.
[7] U.K. Mudali, A.K. Bhaduri, J.B. Gnanamoorthy, Localised corrosion behaviour of 17–4 PH stainless steel, Materials Science and Technology. 6 (1990) 7. https://doi.org/10.1179/mst.1990.6.5.475.
[8] G. Wranglen, Pitting and sulfide inclusion in steel, Corrosion Science. 14 (1974) 331–349.
[9] J.E. Castle, R. Ke, Studies by auger spectroscopy of pit initiation at the site of inclusions in stainless steel, Corrosion Science. 30 (1990) 409–428. https://doi.org/10.1016/0010-938X(90)90047-9.
[10] J.H. Park, Y. Kang, Inclusions in Stainless Steels − A Review, Steel Research International. 88 (2017) 1700130. https://doi.org/10.1002/srin.201700130.
[11] M.A. Baker, J.E. Castle, The initiation of pitting corrosion at MnS inclusions, Corrosion Science. 34 (1993) 667–682. https://doi.org/10.1016/0010-938X(93)90279-P.
[12] E.G. Webb, R.C. Alkire, Pit Initiation at Single Sulfide Inclusions in Stainless Steel, Journal of The Electrochemical Society. 149 (2002) B272. https://doi.org/10.1149/1.1474430.
[13] D.E. Williams, Elucidation of a Trigger Mechanism for Pitting Corrosion of Stainless Steels Using Submicron Resolution Scanning Electrochemical and Photoelectrochemical Microscopy, Journal of The Electrochemical Society. 145 (1998) 2664. https://doi.org/10.1149/1.1838697.
[14] R. Ke, Surface Analysis of Corrosion Pits Initiated at MnS Inclusions in 304 Stainless Steel, Journal of The Electrochemical Society. 139 (1992) 1573. https://doi.org/10.1149/1.2069458.
[15] J. Stewart, D.E. Williams, The initiation of pitting corrosion on austenitic stainless steel: on the role and importance of sulphide inclusions, Corrosion Science. 33 (1992) 457–474. https://doi.org/10.1016/0010-938X(92)90074-D.
[16] E.G. Webb, T. Suter, R.C. Alkire, Microelectrochemical Measurements of the Dissolution of Single MnS Inclusions, and the Prediction of the Critical Conditions for Pit Initiation on Stainless Steel, Journal of The Electrochemical Society. 148 (2001) B186. https://doi.org/10.1149/1.1360205.
[17] D.E. Williams, Y.Y. Zhu, Explanation for Initiation of Pitting Corrosion of Stainless Steels at Sulfide Inclusions, Journal of The Electrochemical Society. 147 (2000) 1763. https://doi.org/10.1149/1.1393431.
[18] Q. Meng, G.S. Frankel, H.O. Colijn, S.H. Goss, Stainless-steel corrosion and MnS inclusions, Nature. 424 (2003) 389–390. https://doi.org/10.1038/424389b.
[19] Q. Meng, G.S. Frankel, H.O. Colijn, S.H. Goss, High-Resolution Characterization of the Region Around Manganese Sulfide Inclusions in Stainless Steel Alloys, CORROSION. 60 (2004) 346–355. https://doi.org/10.5006/1.3287741.
[20] C.T. Kwok, H.C. Man, F.T. Cheng, Cavitation erosion and pitting corrosion of laser surface melted stainless steels, Surface and Coatings Technology. 99 (1998) 295–304. https://doi.org/10.1016/S0257-8972(97)00624-5.
[21] C. Carboni, P. Peyre, G.B.E. Ranger, C. Lemaitre, Influence of high power diode laser surface melting on the pitting corrosion resistance of type 316L stainless steel, Journal of Materials Science. (2002) 3715–3723.
[22] N. Guo, M.C. Leu, Additive manufacturing: technology, applications and research needs, Frontiers of Mechanical Engineering. 8 (2013) 215–243. https://doi.org/10.1007/s11465-013-0248-8.
[23] J.-P. Kruth, M.-C. Leu, T. Nakagawa, Progress in additive manufacturing and rapid prototyping, Cirp Annals. 47 (1998) 525–540. https://doi.org/10.1016/S0007-8506(07)63240-5.

[24] L.E. Murr, E. Martinez, K.N. Amato, S.M. Gaytan, J. Hernandez, D.A. Ramirez, P.W. Shindo, F. Medina, R.B. Wicker, Fabrication of Metal and Alloy Components by Additive Manufacturing: Examples of 3D Materials Science, Journal of Materials Research and Technology. 1 (2012) 42–54. https://doi.org/10.1016/S2238-7854(12)70009-1.
[25] T. Niendorf, S. Leuders, A. Riemer, H.A. Richard, T. Tröster, D. Schwarze, Highly Anisotropic Steel Processed by Selective Laser Melting, Metallurgical and Materials Transactions B. 44 (2013) 794–796. https://doi.org/10.1007/s11663-013-9875-z.
[26] S. Dadbakhsh, B. Vrancken, J.-P. Kruth, J. Luyten, J. Van Humbeeck, Texture and anisotropy in selective laser melting of NiTi alloy, Materials Science and Engineering: A. 650 (2016) 225–232. https://doi.org/10.1016/j.msea.2015.10.032.
[27] H.K. Rafi, D. Pal, N. Patil, T.L. Starr, B.E. Stucker, Microstructure and Mechanical Behavior of 17-4 Precipitation Hardenable Steel Processed by Selective Laser Melting, Journal of Materials Engineering and Performance. 23 (2014) 4421–4428. https://doi.org/10.1007/s11665-014-1226-y.
[28] S. Cheruvathur, E.A. Lass, C.E. Campbell, Additive Manufacturing of 17-4 PH Stainless Steel: Post-processing Heat Treatment to Achieve Uniform Reproducible Microstructure, JOM. 68 (2016) 930–942. https://doi.org/10.1007/s11837-015-1754-4.
[29] M. Alnajjar, F. Christien, K. Wolski, C. Bosch, Evidence of austenite by-passing in a stainless steel obtained from laser melting additive manufacturing, Additive Manufacturing. (2018) 187–195. https://doi.org/10.1016/j.addma.2018.11.004.
[30] Q. Chao, V. Cruz, S. Thomas, N. Birbilis, P. Collins, A. Taylor, P.D. Hodgson, D. Fabijanic, On the enhanced corrosion resistance of a selective laser melted austenitic stainless steel, Scripta Materialia. 141 (2017) 94–98. https://doi.org/10.1016/j.scriptamat.2017.07.037.
[31] M.J.K. Lodhi, K.M. Deen, W. Haider, Corrosion behavior of additively manufactured 316L stainless steel in acidic media, Materialia. (2018) 1–11. https://doi.org/10.1016/j.mtla.2018.06.015.
[32] S.-H. Sun, T. Ishimoto, K. Hagihara, Y. Tsutsumi, T. Hanawa, T. Nakano, Excellent mechanical and corrosion properties of austenitic stainless steel with a unique crystallographic lamellar microstructure via selective laser melting, Scripta Materialia. 159 (2019) 89–93. https://doi.org/10.1016/j.scriptamat.2018.09.017.
[33] M.R. Stoudt, R.E. Ricker, E.A. Lass, L.E. Levine, Influence of Postbuild Microstructure on the Electrochemical Behavior of Additively Manufactured 17-4 PH Stainless Steel, JOM. 69 (2017) 506–515. https://doi.org/10.1007/s11837-016-2237-y.
[34] R.F. Schaller, J.M. Taylor, J. Rodelas, E.J. Schindelholz, Corrosion Properties of Powder Bed Fusion Additively Manufactured 17-4 PH Stainless Steel, CORROSION. 73 (2017) 796–807. https://doi.org/10.5006/2365.
[35] F. Christien, D. Fortes, M. Alnajjar, M. Telling, Solid state phase transformations at very high temperature in a martensitic stainless steel, STFC ISIS Neutron and Muon Source. (2018). https://doi.org/10.5286/ISIS.E.90682570.
[36] G.R. Stibitz, Energy of lattice distortion, Physical Review. 49 (1936) 859–891.
[37] F.E. Haworth, Energy of Lattice Distortion in Cold Worked Permalloy, Phys. Rev. 52 (1937) 613–620. https://doi.org/10.1103/PhysRev.52.613.
[38] F. Christien, M.T.F. Telling, K.S. Knight, R. Le Gall, A method for the monitoring of metal recrystallization based on the in-situ measurement of the elastic energy release using neutron diffraction, Review of Scientific Instruments. 86 (2015) 053901. https://doi.org/10.1063/1.4919414.
[39] A.C. Larson, R.B. Von Dreele, General structure analysis system, Los Alamos National Laboratory Report, 1994.
[40] B.H. Toby, EXPGUI , a graphical user interface for GSAS, J Appl Crystallogr. 34 (2001) 210–213. https://doi.org/10.1107/S0021889801002242.

[41] T. Nyyssönen, M. Isakov, P. Peura, V.-T. Kuokkala, Iterative Determination of the Orientation Relationship Between Austenite and Martensite from a Large Amount of Grain Pair Misorientations, Metall and Mat Trans A. 47 (2016) 2587–2590. https://doi.org/10.1007/s11661-016-3462-2.
[42] Y. Sun, R.J. Hebert, M. Aindow, Effect of heat treatments on microstructural evolution of additively manufactured and wrought 17-4PH stainless steel, Materials & Design. 156 (2018) 429–440. https://doi.org/10.1016/j.matdes.2018.07.015.
[43] S. Vunnam, A. Saboo, C. Sudbrack, T.L. Starr, Effect of powder chemical composition on the as-built microstructure of 17-4 PH stainless steel processed by selective laser melting, Additive Manufacturing. 30 (2019) 100876. https://doi.org/10.1016/j.addma.2019.100876.
[44] F. Christien, M.T.F. Telling, K.S. Knight, Neutron diffraction in situ monitoring of the dislocation density during martensitic transformation in a stainless steel, Scripta Materialia. 68 (2013) 506–509. https://doi.org/10.1016/j.scriptamat.2012.11.031.
[45] R. Coppola, P. Lukáš, P. Mikula, M. Vrána, Neutron-diffraction line broadening in a tempered martensitic steel for fusion reactors, Physica B: Condensed Matter. 241–243 (1997) 1261–1263. https://doi.org/10.1016/S0921-4526(97)00841-7.
[46] K. Macek, P. Lukáš, J. Janovec, P. Mikula, P. Strunz, M. Vrána, M. Zaffagnini, Austenite content and dislocation density in electron-beam welds of a stainless maraging steel, Materials Science and Engineering: A. 208 (1996) 131–138. https://doi.org/10.1016/0921-5093(95)10047-4.
[47] A.U. Malik, S.A. Fozan, Crevice corrosion behavior of AISI 316L SS in arabian gulf seawater, 1993.
[48] B. Baroux, Y. Bréchet, J. Charles, La corrosion des métaux passivité et corrosion localisée, L'Usine nouvelle : Dunod, Paris, 2014.
[49] M.B. Ives, Metallography of pitting corrosion, Materials Characterization. 28 (1992) 257–270. https://doi.org/10.1016/1044-5803(92)90015-A.
[50] V. Vignal, S. Ringeval, S. Thiébaut, K. Tabalaiev, C. Dessolin, O. Heintz, F. Herbst, R. Chassagnon, Influence of the microstructure on the corrosion behaviour of low-carbon martensitic stainless steel after tempering treatment, Corrosion Science. 85 (2014) 42–51. https://doi.org/10.1016/j.corsci.2014.03.036.
[51] S.G. Wang, C.B. Shen, K. Long, H.Y. Yang, F.H. Wang, Z.D. Zhang, Preparation and Electrochemical Corrosion Behavior of Bulk Nanocrystalline Ingot Iron in HCl Acid Solution, J. Phys. Chem. B. 109 (2005) 2499–2503. https://doi.org/10.1021/jp046297v.
[52] B. Hadzima, M. Janeček, Y. Estrin, H.S. Kim, Microstructure and corrosion properties of ultrafine-grained interstitial free steel, Materials Science and Engineering: A. 462 (2007) 243–247. https://doi.org/10.1016/j.msea.2005.11.081.
[53] K.D. Ralston, N. Birbilis, Effect of Grain Size on Corrosion: A Review, CORROSION. 66 (2010) 075005-075005–13. https://doi.org/10.5006/1.3462912.
[54] M. Pisarek, P. Kędzierzawski, M. Janik-Czachor, K.J. Kurzydłowski, Effect of hydrostatic extrusion on passivity breakdown on 303 austenitic stainless steel in chloride solution, J Solid State Electrochem. 13 (2009) 283–291. https://doi.org/10.1007/s10008-007-0488-9.
[55] Y. Hao, B. Deng, C. Zhong, Y. Jiang, J. Li, Effect of surface mechanical attrition treatment on corrosion behavior of 316 stainless steel, J. Iron Steel Res. Int. 16 (2009) 68–72. https://doi.org/10.1016/S1006-706X(09)60030-3.
[56] B. Vuillemin, X. Philippe, R. Oltra, V. Vignal, L. Coudreuse, L.C. Dufour, E. Finot, SVET, AFM and AES study of pitting corrosion initiated on MnS inclusions by microinjection, Corrosion Science. 45 (2003) 1143–1159. https://doi.org/10.1016/S0010-938X(02)00222-6.
[57] H. Krawiec, V. Vignal, O. Heintz, R. Oltra, J.-M. Olive, Influence of the Chemical Dissolution of MnS Inclusions on the Electrochemical Behavior of Stainless Steels, Journal of The Electrochemical Society. 152 (2005) B213. https://doi.org/10.1149/1.1924172.

[58] S.-T. Kim, Y.-S. Park, Effect of Sulfur Content of Copper-Containing Austenitic Stainless Steels on Corrosion Behavior in Concentrated Sulfuric Acid—Part 2, CORROSION. 64 (2008) 496–508. https://doi.org/10.5006/1.3278486.
[59] A. Elbiache, P. Marcus, The role of molybdenum in the dissolution and the passivation of stainless steels with adsorbed sulphur, Corrosion Science. 33 (1992) 261–269. https://doi.org/10.1016/0010-938X(92)90150-2.
[60] P. Marcus, A. Teissier, J. Oudar, The influence of sulphur on the dissolution and the passivation of a nickel-iron alloy—I. electrochemical and radiotracer measurements, Corrosion Science. 24 (1984) 259–268. https://doi.org/10.1016/0010-938X(84)90012-X.
[61] J. Oudar, P. Marcus, Role of adsorbed sulphur in the dissolution and passivation of nickel and nickel-sulphur alloys, Applications of Surface Science. 3 (1979) 48–67. https://doi.org/10.1016/0378-5963(79)90060-6.
[62] G.S. Eklund, Initiation of Pitting at Sulfide Inclusions in Stainless Steel, J. Electrochem. Soc. 121 (1974) 467. https://doi.org/10.1149/1.2401840.
[63] N. Hara, K. Hirabayashi, Y. Sugawara, I. Muto, Improvement of Pitting Corrosion Resistance of Type 316L Stainless Steel by Potentiostatic Removal of Surface MnS Inclusions, International Journal of Corrosion. 2012 (2012) 1–6. https://doi.org/10.1155/2012/482730.
[64] S. Hastuty, E. Tada, A. Nishikata, Y. Tsutsumi, T. Hanawa, Improvement of Pitting Corrosion Resistance of Type 430 Stainless Steel by Electrochemical Treatments in a Concentrated Nitric Acid, ISIJ Int. 54 (2014) 199–205. https://doi.org/10.2355/isijinternational.54.199.
[65] N. Alonso-Falleiros, S. Wolynec, Correlation between Corrosion Potential and Pitting Potential for AISI 304L Austenitic Stainless Steel in 3.5% NaCl Aqueous Solution, Materials Research. 5 (2002) 77–84. https://doi.org/10.1590/S1516-14392002000100013.
[66] E.A. Ferreira, R.D. Noce, C.S. Fugivara, A.V. Benedetti, Evaluation of 316L Stainless Steel Corrosion Resistance in Solution Simulating the Acid Hydrolysis of Biomass, Journal of The Electrochemical Society. 158 (2011) C95. https://doi.org/10.1149/1.3554728.
[67] H. Franzen, C. Sterner, The X-ray photoelectron spectra of MnS, MnSe, and MnTe, Journal of Solid State Chemistry. 25 (1978) 227–230. https://doi.org/10.1016/0022-4596(78)90107-X.
[68] P. Tiwari, G. Malik, R. Chandra, Phase-dependent structural and electrochemical properties of single crystalline MnS thin films deposited by DC reactive sputtering, Journal of Applied Physics. 124 (2018) 195106. https://doi.org/10.1063/1.5053875.
[69] C. Duret-Thual, D. Costa, W.P. Yang, P. Marcus, The role of thiosulfates in the pitting corrosion of Fe-17Cr alloys in neutral chloride solution: Electrochemical and XPS study, Corrosion Science. 39 (1997) 913–933. https://doi.org/10.1016/S0010-938X(97)81158-4.
[70] W.Y. Lai, W.Z. Zhao, Z.F. Yin, J. Zhang, EIS and XPS studies on passive film of AISI 304 stainless steel in dilute sulfuric acid solution: Passive film of AISI 304 stainless steel, Surf. Interface Anal. 44 (2012) 418–425. https://doi.org/10.1002/sia.3819.
[71] P. Marcus, J.M. Grimal, The antagonistic roles of chromium and sulphur in the passivation of Ni□Cr□Fe alloys studied by XPS and radiochemical techniques, Corrosion Science. 31 (1990) 377–382. https://doi.org/10.1016/0010-938X(90)90134-Q.
[72] M.C. Biesinger, B.R. Hart, R. Polack, B.A. Kobe, R.St.C. Smart, Analysis of mineral surface chemistry in flotation separation using imaging XPS, Minerals Engineering. 20 (2007) 152–162. https://doi.org/10.1016/j.mineng.2006.08.006.
[73] A. Galtayries, C. Cousi, S. Zanna, P. Marcus, SO2 adsorption at room temperature on Ni(111) surface studied by XPS, Surf. Interface Anal. 36 (2004) 997–1000. https://doi.org/10.1002/sia.1821.
[74] K. Rokosz, T. Hryniewicz, F. Simon, S. Rzadkiewicz, Comparative XPS analyses of passive layers composition formed on Duplex 2205 SS after standard and high-current-density electropolishing,

Tehnicki Vjesnik - Technical Gazette. 23 (2016) 731–735. https://doi.org/10.17559/TV-20141107094438.